JOURNAL OF
SYNCHROTRON
RADIATION

ISSN 1600-5775

Side-bounce beamlines using single-reflection diamond monochromators at Cornell High Energy Synchrotron Source

Stanislav Stoupin,[a]*‡ Thomas Krawczyk,[a] David Sagan,[a] Alexander Temnykh,[a] Louisa Smieska,[a] Arthur Woll,[a] Jacob Ruff,[a] Aaron Lyndaker,[a] Alan Pauling,[a] Brendan P. Croom[b] and Edward B. Trigg[b]

[a]Cornell High Energy Synchrotron Source, Cornell University, Ithaca, New York, USA, and [b]Materials and Manufacturing Directorate, Air Force Research Laboratory, Wright-Patterson Air Force Base, Dayton, Ohio, USA. *Correspondence e-mail: stoupin1@llnl.gov

Received 10 July 2020
Accepted 2 February 2021

Edited by A. Momose, Tohoku University, Japan

‡ Now at Lawrence Livermore National Laboratory, Livermore, California, USA.

Keywords: X-ray monochromators; diamond; beamlines.

Supporting information: this article has supporting information at journals.iucr.org/s

The design and implementation of new beamlines featuring side-bounce (single-reflection) diamond monochromators at Cornell High Energy Synchrotron Source (CHESS) are described. Undulator radiation is monochromated using an interchangeable set of diamond crystal plates reflecting radiation in the horizontal (synchrotron) plane, where each crystal plate is set to one of the low-index Bragg reflections (111, 220, 311 and 400) in either Bragg or Laue reflection geometries. At the nominal Bragg angle of 18° these reflections deliver monochromated X-rays with photon energies of 9.7, 15.9, 18.65 and 22.5 keV, respectively. An X-ray mirror downstream of the diamond monochromator is used for rejection of higher radiation harmonics and for initial focusing of the monochromated beam. The characteristics of the X-ray beam entering the experimental station were measured experimentally and compared with the results of simulations. A reasonable agreement is demonstrated. It is shown that the use of selected high-dislocation-density 'mosaic' diamond single-crystal plates produced using the chemical vapor deposition method yields a few-fold enhancement in the flux density of the monochromated beam in comparison with that delivered by perfect crystals under the same conditions. At present, the Functional Materials Beamline at CHESS, which is used for time-resolved *in situ* characterization of soft materials during processing, has been outfitted with the described setup.

1. Introduction

A single-reflection high-heat-load crystal monochromator is a well known concept for monochromatization of synchrotron radiation (Lennie *et al.*, 2007; Jiang *et al.*, 2012; Gomez *et al.*, 2018). The monochromator selects a narrow energy bandwidth from a wide polychromatic (bending magnet, wiggler) or multi-harmonic (undulator) spectrum of incoming synchrotron radiation using a particular Bragg reflection. The monochromated X-ray beam can be used for a variety of experiments as long as the chosen photon energy yields a good signal contrast, and energy tunability in a wide range ($\Delta E \gtrsim 10$ eV) is not required. Applications are found using X-ray imaging, X-ray fluorescence and many methods of X-ray scattering.

The single-reflection approach has a number of advantages. For one, a convenient space-preserving beamline layout can be implemented, especially if the X-rays are reflected in the horizontal plane (the so-called side-bounce configuration). Additionally, monochromator motion control is relatively straightforward due to relaxed angular tolerances. Losses in diffraction efficiency due to heat-load-induced strain of the

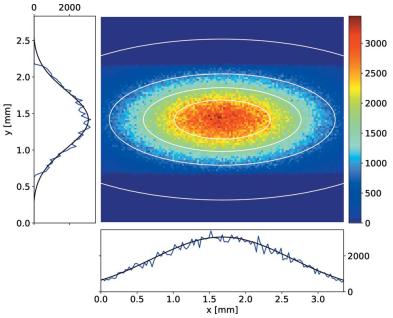

https://doi.org/10.1107/S160057752100120X

crystal lattice are minimal for a single-reflection monochromator compared with a double-crystal monochromator, where the efficiency may be reduced because the second (thermally undistorted) crystal reflects the divergent beam emanating from the distorted first crystal (Bilderback *et al.*, 2000). Also, for a single-reflection monochromator radiation heat-load mitigation is simplified (*e.g.* water cooling versus cryocooling), especially if robust single crystals with low X-ray absorption and high thermal conductivity like diamond are employed. These properties of the monochromator's crystal are also essential for beam multiplexing solutions at synchrotrons and XFELs (Als-Nielsen *et al.*, 1994; Grübel *et al.*, 1996; Juanhuix *et al.*, 2014; Dippel *et al.*, 2015; Zhu *et al.*, 2014).

In this work, the design, implementation and performance characteristics of two new side-bounce beamlines at the Cornell High Energy Synchrotron Source (CHESS) are reported. These beamlines were built as part of the recent facility upgrade (CHESS-U). Each of the two beamlines, designated beamline 2B and beamline 3B, is equipped with an individual undulator source (Temnykh *et al.*, 2013, 2016) and a diamond multi-crystal side-bounce monochromator operating at a set of four fixed photon energies. One of the main challenges for the beamline implementation was the lack of a stable supply of large diamond plates of high crystal quality [*i.e.* crystals produced using the high-pressure high-temperature method (HPHT)]. Instead, selected commercially available chemical vapor deposited (CVD) single crystals were used. These crystals featured working regions characterized by a uniformly high dislocation density to increase the reflection intensities, as well as a minimal effective crystal-lattice curvature to prevent unpredictable focusing of the reflected beam and thus any possible substantial increase in the size of the beam profile (Stoupin *et al.*, 2019*a*).

The key characteristics of the monochromated beam (photon flux, energy bandwidth and dimensions of the beam profile) were measured and compared with the results of ray-tracing simulations for perfect crystals. Our analysis indicates that selected imperfect CVD crystals operating in the Laue (transmission) geometry yield a few-fold enhancement in the flux density of the reflected beam. This increase, leading to a relative energy resolution of about $\Delta E/E \simeq 10^{-3}$, can be tolerated by a large number of experiments. The characteristic sizes of the profiles of CVD diamond-reflected beams in the experimental station were found to be manageable (*e.g.* 3 mm × 5 mm), and even beneficial in some experiments (*e.g.* an increased field of view for X-ray radiography). One of the newly constructed beamlines was chosen to host the Functional Materials program at CHESS, where X-ray scattering and X-ray imaging methods are used to perform materials research.

2. Beamline layout and operating principles

The layout of the side-bounce beamlines is shown schematically in Fig. 1. Fig. 1(*a*) shows the top view illustrating the horizontal (synchrotron) plane, while Figs. 1(*b*) and 1(*c*) show the side views.

Table 1
X-ray source characteristics.

R.m.s. horizontal size, s_x	0.57 mm
R.m.s. horizontal divergence, s_x'	53 µrad
R.m.s. vertical size, s_y	0.028 mm
R.m.s. vertical divergence, s_y'	16 µrad

The X-ray source (*S*) has finite dimensions and finite angular divergence. The source characteristics, calculated using the *SPECTRA* program (Tanaka & Kitamura, 2001) taking into account the parameters of the storage ring (Shanks *et al.*, 2019) and the parameters of the undulator (Temnykh *et al.*, 2013, 2016), are summarized in Table 1.

The divergent X-ray beam (gray in Fig. 1) emitted by the source is incident on the diamond crystal plate (C) of the monochromator (a symmetric Laue reflection is illustrated). The sizes of individual components, and the divergence of the X-ray beam, are exaggerated for clarity. The reflected beam (aqua) is converging, which illustrates the effect of pseudo-focusing in the Laue geometry (Sanchez del Rio *et al.*, 1995). The beam is either bypassed [Fig. 1(*b*)] or reflected [Fig. 1(*c*)] by the harmonic rejection mirror (M) and intercepted by the area detector (AD) placed in the experimental station at a distance corresponding to a nominal sample location. The undulator beam is restricted by a vertical fixed aperture $A_{\rm V}$ = 1 mm placed just upstream of the monochromator. There is no beam-limiting aperture in the horizontal direction. The monochromated beam can be shaped using two sets of variable slits. The first set ($S^0_{\rm H} \times S^0_{\rm V}$) is placed just downstream of the monochromator while the second set ($S^1_{\rm H} \times S^1_{\rm V}$) is placed near the sample position (upstream of the area detector). The horizontal slit blades are shown schematically in Fig. 1(*a*). The vertical aperture and vertical slit blades are shown schematically in Fig. 1(*b*) but omitted from Fig. 1(*c*) for clarity.

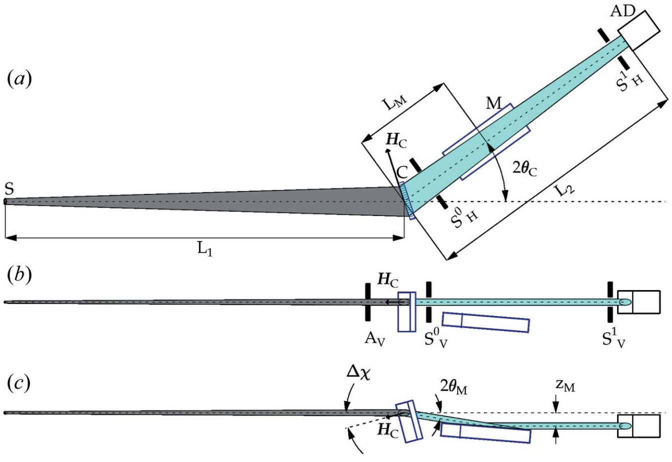

Figure 1
Beamline layout (see text for details). (*a*) Top view (horizontal/synchrotron plane), (*b*) side view of the mode with the beam bypassing the X-ray mirror, and (*c*) side view of the mode with the beam reflected from the mirror.

Table 2
Beamline distances (m).

	Distance		
Beamline	L_1	L_2	L_M
2B	16.95	12.0	1.15
3B	16.84	8.0	1.25

Table 3
Main design characteristics of the monochromator for beamline 3B.

Reflection	E_X (keV)	Geometry	ΔE_t (eV)
111	9.742	Bragg	3.75
220	15.907	Laue	6.08
131	18.652	Laue	7.13
400	22.496	Laue	8.59

To preserve the original beam direction after reflection from the mirror, the scattering plane of the reflection is tilted by adjusting the monochromator crystal's azimuthal angle by an amount

$$\Delta\chi \simeq \frac{\theta_M}{\sin\theta_C}, \qquad (1)$$

where θ_M is the angle of incidence to the X-ray mirror and θ_C is the Bragg angle of the reflection. A value of 18° was chosen by design for each of the two beamlines. This arrangement leads to a vertical offset of the beam by an amount

$$z_M = L_M \tan 2\theta_M, \qquad (2)$$

where L_M is the distance from the crystal to the mirror. Values for L_M, along with the source-to-monochromator distance L_1 and monochromator-to-sample distance L_2, are given in Table 2 for the two beamlines 2B and 3B. Given typical values for θ_M of a few milliradians (the optimized value depends on the working photon energy), the resulting offset is a few millimetres. While the mirror positions remain fixed, the mirror can be bypassed by an adjustment of $\Delta\chi$ of the crystal. This has been found useful for diagnostic purposes during beamline alignment and commissioning.

The side-bounce monochromator of each beamline holds four diamond crystal plates aligned for four different reflections which correspond to four photon energies of the Bragg reflected beam. Switching between the reflections requires translation and angular adjustment of the water-cooled copper block holding the crystal plates. For each reflection, the positions of the monochromator and mirror are stored. The saved positions can be optimized and updated during beamline alignment. After the optimization, switching between different reflections/energies is achieved by a single software command. More details on the monochromator are presented in Section 3.

3. Side-bounce diamond monochromator

3.1. Optomechanical design

The four diamond reflections chosen for the high-heat-load monochromator on the side-bounce beamlines are 111, 220, 131 and 400. The photon energies corresponding to the nominal Bragg angles for these reflections are shown in Table 3. The table also shows the values of the energy bandwidths estimated as

$$\Delta E_t = E_X\left[\left(\Delta\psi\cot\theta_C\right)^2 + \varepsilon_{hkl}^2\right]^{1/2}, \qquad (3)$$

where $\Delta\psi \simeq 124\,\mu\text{rad}$ is the divergence of the incident undulator beam and ε_{hkl} is the intrinsic relative energy width of a given diamond reflection (perfect crystal, π-polarization). Both values are taken as full widths at half-maximum (FWHM). Estimates by equation (3) are valid for the case of nearly perfect crystals and represent the total energy bandwidth of the reflected beam across the FWHM size.

Each of the reflections required a separate diamond crystal plate. The arrangement of the plates is shown schematically in Fig. 2(*a*) for the 3B beamline monochromator. The undulator beam (gray) is incident on a particular reflector. The reflected beam is shown in aqua. In the figure, the 111 reflector is being used. This reflector has a slightly asymmetric Bragg geometry

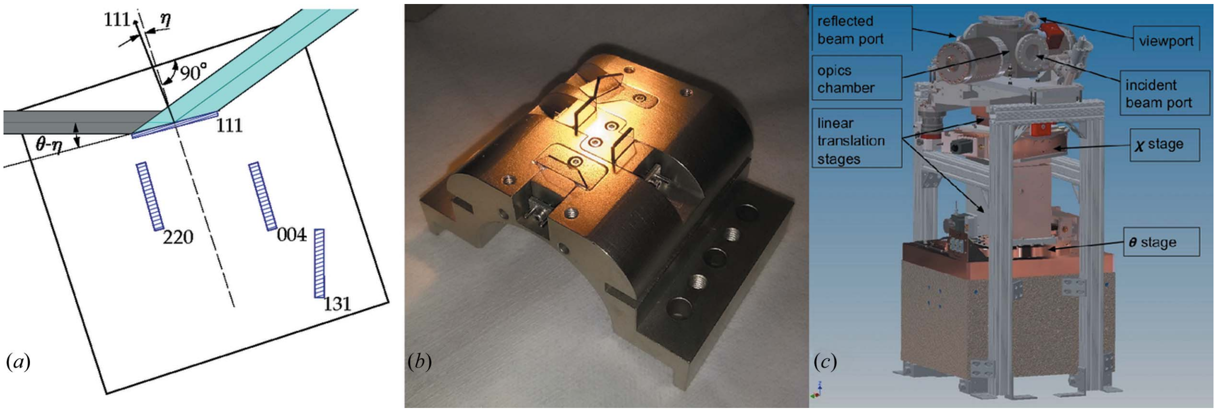

Figure 2
Optomechanical design of the monochromator. (*a*) Optical arrangement of the diamond plates for the 3B beamline with respect to the incident (gray) and reflected (aqua) beams and the block holding the plates. (*b*) A picture of the block (made of nickel-plated copper) holding the diamond plates (3B beamline). (*c*) Mechanical assembly of the monochromator (see text for details).

denoted by the asymmetry angle η. A rectangular copper block holding the crystals is tilted at θ_C with respect to the incident beam. The edges of the block serve as an angular reference for the alignment of the crystal plates on the block. The schematic for the 2B beamline is similar except that all reflectors are aligned in Laue (transmission) geometry.

Fig. 2(*b*) shows a picture of the block holding the diamond plates. The water-cooled block, which is removable, is made of nickel-plated copper. The reflectors are installed using adjustable clamps, which support the lower portion (approximately half) of each plate and restrain each plate's motion with only minimal applied pressure. The lower portions of the plates are in thermal contact with the block using InGa eutectic (viscous liquid at room temperature), while the upper (working) portions are exposed to the undulator X-ray beam. The basic idea of the described crystal-mounting scheme was based on a preliminary design of diamond monochromators at the Linac Coherent Light Source (LCLS). This preliminary design, however, was not adopted at the LCLS in favor of an alternative solution (Stoupin *et al.*, 2014).

Fig. 2(*c*) shows the mechanical assembly of the monochromator. The block holding the reflectors is placed, via bellows, in a vacuum chamber connected to the supporting structure. The chamber can be translated in the horizontal (synchrotron) plane using a pair of linear translation stages (x and y directions). These translations enable centering of a particular reflector on the incident beam. A viewport in the chamber enables video monitoring of luminescence in the diamond plates excited by the incident X-ray beam, thus providing visual alignment confirmation. The linear translation stages are installed on a segmented circle stage, which performs azimuthal rotation (χ) of the crystal. The segmented circle stage is placed on an elevation stage (z direction) having a range of motion which permits complete retraction of the plates from the incident beam. Finally, at the base of the assembly is the rotation stage controlling the scattering angle (θ). To accommodate the copper lines that supply the cooling water, the angular ranges of motion for χ and θ are limited to about ±5°. Therefore, accurate placement of the reflectors on the block is essential.

3.2. Choice of the diamond crystals

Based upon the horizontal source size and the divergence parameters of the X-ray source, the nominal horizontal size of the incident X-ray beam at the monochromator's location is calculated to be about $b_x \simeq 2.5$ mm (FWHM). Therefore, at the Bragg angle of $\theta_C = 18°$, the length of the crystal plate required to intercept the beam size in the Bragg geometry is $l_x = b_x / \sin\theta_C = 8.1$ mm. High-quality HPHT diamond crystal plates of such lengths and a specified crystallographic surface orientation are not widely available. The advantages of using high-quality (nearly perfect) crystals in the Bragg geometry are wavefront preservation and very high reflectivity (nearly 100% for diamond). Fortunately, it was possible to acquire one large plate with a close to 111 surface orientation. The 0.5 mm thick plate was fabricated by New Diamond Technology (Russia). It was characterized with rocking-curve X-ray topography in the double-crystal nondispersive configuration using an Si 220 asymmetric beam conditioner (Stoupin *et al.*, 2016) and a photon energy of ~8 keV on the 1-BM beamline (Macrander *et al.*, 2016) at the Advanced Photon Source (Argonne National Laboratory). Rocking-curve topographs showing peak position[1] $\delta\theta_m$ and curve width[2] $\Delta\theta$ are presented in Fig. 3. The dashed rectangle (~8.5 × 1.8 mm) shows a region of reasonably good quality. The variation in the curve width in this region was found to be $\lesssim 0.5$ µrad root-mean-square (r.m.s.) and the variation in the peak position across the region was about 3 µrad (excluding edge effects). The surface orientation was found to be 3.3° off the (111) plane (polishing miscut). The misorientation direction is shown in Fig. 3 using the projection of the 111 reciprocal vector (black arrow) on the crystal surface. The crystal was employed as the 111 reflector (photon energy 9.74 keV) in the monochromator of beamline 3B.

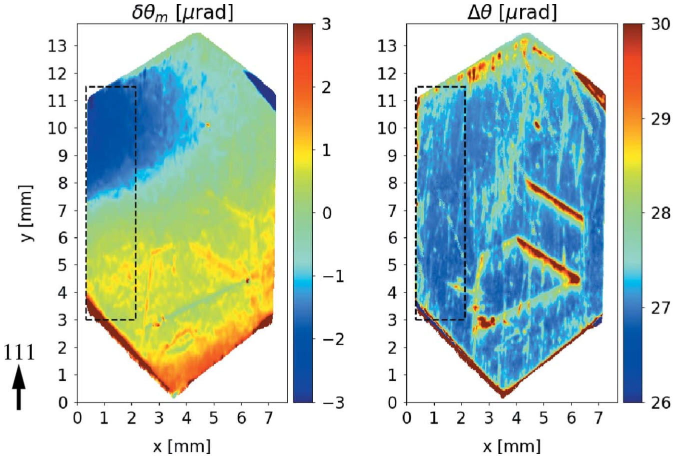

Figure 3
Rocking-curve topographs for the large diamond plate, which was chosen as the 111 Bragg reflector in the high-heat-load monochromator of beamline 3B. The topographs show peak position ($\delta\theta_m$) and curve width ($\Delta\theta$). The dashed rectangle (~8.5 × 1.8 mm) shows a region of reasonably good quality. The projection of the 111 reciprocal vector on the surface of the plate is shown with a black arrow (3.3° miscut).

CVD single-crystal plates procured from Applied Diamond were used for all other reflectors. These plates featured lateral sizes of 7 × 7 mm (square), a thickness of 1 mm and a uniform high dislocation density of $\rho \gtrsim 1 \times 10^6$ cm^{-2}. The dislocation density was greater than what conventional X-ray topography techniques can resolve (Bowen & Tanner, 1998), as confirmed in our prior study (Stoupin *et al.*, 2019*a*), which included white-beam Laue X-ray topography. This resulted in an increase in the reflection intensities due to the enhancement of the effective intrinsic energy bandwidth (Stoupin *et al.*, 2018, 2019*b*). The CVD plates were of two distinct crystallographic orientations: plates of the first type had a nominal (110) edge

---

[1] The peak position was determined as the average of the angular positions (mid-point) of the left slope and right slope of the curve; the slope positions correspond to the half-maximum level.

[2] The curve width was calculated as the difference between the slope positions, thus representing full width at half-maximum.

orientation (*i.e.* 110 reciprocal vector normal to the edge of the plate), while plates of the second type had a nominal (100) edge orientation. For plates of both types, the nominal orientation of the working 7 × 7 mm surface was (001). The average crystallographic orientation was measured using a Multiwire X-ray back-reflection instrument at Cornell Center for Materials Research. The precision of this instrument was approximately 0.2°. The measured angular deviations from the nominal orientation did not exceed 3°. The measured angular deviations were taken into account during initial alignment of the plates on the copper block. To achieve a convenient arrangement of the plates with respect to the nominal horizontal and vertical directions of the beamline layout, the 111 and 220 Laue reflectors were of the first type [(110)-edge orientation], while the 131 and 400 reflectors were of the second type [(100)-edge orientation]. In this scheme, orientation of the 131 reflector on the block required an azimuthal rotation of ∼18° with respect to the top surface of the block, as illustrated in Fig. 2(*b*) (the edge of the 131 reflector is tilted with respect to the top surface of the block). Selection of the best crystal plates was performed using X-ray rocking-curve topography (Stoupin *et al.*, 2019*a*). Maps of the effective radius of curvature in the scattering plane were calculated using spline interpolation of the rocking-curve peak position across the plates. Plates with working regions of relatively large effective radius of curvature ($R_0 \gtrsim$ 30–70 m) were selected. This criterion was used to prevent defocusing due to an unknown effective lattice curvature and the related substantial increase in the size of the reflected beam.

4. Beamline characterization and simulation

4.1. Experiment and simulation details

In this work we report the results of characterization on beamline 3B due to more detailed measurements conducted on this beamline. The results of studies of the CVD diamond reflectors on beamline 2B were found to be similar, bearing no contradiction to our conclusions. The characterization was performed while the storage ring was operated at a positron current of 50 mA, generating a substantial heat load for the primary optical components (the maximum operational current is set at 200 mA). No indication of a substantial change in the monochromator's performance was found during more recent tests conducted at 125 mA.

Profiles of the monochromated beams were imaged using the area detector (AD, as shown in Fig. 1). The adjustable slits S_0 and S_1 were fully open. An attenuator (a stack of Si wafers) was placed in front of the area detector to prevent image saturation. With the beam bypassing the X-ray mirror [*cf.* Fig. 1(*a*)], it was found that the signal on the detector was affected by higher radiation harmonics. Therefore, interpretation of images collected in this mode requires caution.

X-ray flux characterization was performed using an N_2-filled ionization chamber of length 6 cm and an online calculator (Revesz, 2007). The mass–energy absorption coefficient taken at the corresponding photon energies (Hubbell & Seltzer, 2004) was assumed as the mechanism responsible for the production of electric current in the ionization chamber.

The slit S_0 openings (gaps) were set to S_H^0 = 2 mm and S_V^0 = 6 mm (essentially not limiting the beam in the vertical direction), while the gaps of slit S_1 were set to 2 mm × 2 mm.

The undulator K parameter was optimized by maximizing the intensity passing through both slits onto the ionization chamber. The radiation bandwidth was measured using a crystal analyzer operating at Si 111 and Si 333 reflections [symmetric Si(111) crystal] using a method developed by Batterman *et al.* (2021).

Ray tracing was performed using *Lux*, which is a program based upon the *BMAD* toolkit (Sagan, 2006) for charged-particle and X-ray simulations. The simulations assumed a Gaussian source with the nominal parameters of Tables 1, 2 and 3. Perfect diamond crystals were modeled with a specified thickness and asymmetry parameters corresponding to the values measured for the actual crystal plates. The aperture A_V and the effective crystal size in the horizontal direction were the beam-limiting apertures in the simulations of the full beam profiles. In the simulations of the X-ray flux, slits S_0 and S_1 (2 mm × 2 mm gaps) were introduced at the corresponding locations. These settings were consistent with the experimental conditions. The measured parameters and those of ray-tracing simulations are summarized in Table 6.

4.2. Diamond 111 Bragg reflector

The data for the 111 reflector represent an important benchmark for evaluation of the beamline performance since, assuming symmetric reflection of a perfect crystal, the radiation wavefront of the reflected beam should be preserved. The beam profile is expected to be that of the corresponding undulator harmonic (Gaussian, to a good approximation), propagated to the observation plate of the detector and clipped by the A_V aperture and by the lateral effective size of the crystal in the horizontal direction (∼2 mm). Therefore, the beam profile is expected to be Gaussian but truncated in the vertical direction (the beam size is expected to be comparable with the vertical aperture size of 1 mm) and, less prominently, truncated in the horizontal direction (due to the much larger horizontal divergence and the source size).

The images of the beam profiles collected for the 111 reflector under different conditions are shown in Fig. 4. In these tests, the mirror was set to θ_M = 3.8 mrad, and the undulator was optimized to achieve maximum flux at its third harmonic. Fig. 4(*a*) shows a profile of the beam bypassing the X-ray mirror. Fig. 4(*b*) shows a profile of the beam reflected from the mirror while the mirror benders' positions are set to minimize the curvature. Fig. 4(*c*) shows a profile of the beam reflected from the mirror while the mirror benders are set to provide best focusing at the detector position. The contour lines represent the two-dimensional Gaussian fits of the profiles, while the side plots show center slices (in the horizontal and vertical directions) of the profiles (blue lines) and the slices of the corresponding Gaussian fits (black lines).

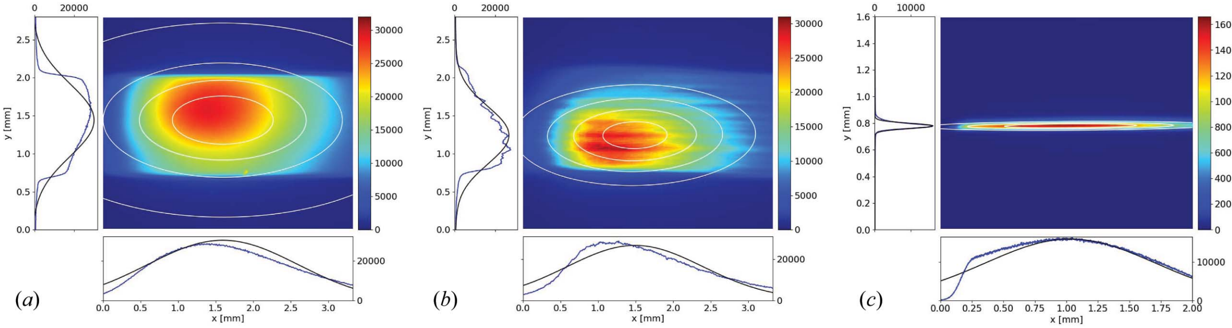

Figure 4
Images of the beam profiles collected with the area detector (AD) for the 111 reflector in different conditions: (*a*) the beam bypasses the X-ray mirror, (*b*) the beam is reflected from the mirror while the positions of the mirror's benders are set to minimize its curvature, and (*c*) the beam is reflected from the mirror while the benders are set to provide best focusing at the detector position.

Table 4
Vertical and horizontal beam sizes (FWHM) for the 111 reflector at the detector position: calculated using equation (4), measured with the monochromated beam both bypassing the mirror and in reflection from it, as well as simulated using ray tracing for a crystal of concave shape with a radius of curvature R = 70 m.

Condition	d_x (mm)	d_y (mm)
Nominal beam	3.36	0.95
Mirror-bypassed beam	2.37	1.13
Mirror-reflected beam	2.14	0.89
Simulation (*BMAD*)	2.29	0.93

The measured beam profiles in Figs. 4(*a*) and 4(*b*) reveal noticeable deviation from the Gaussian shape in both vertical and horizontal directions. The profile in the vertical direction is affected by the mirror's imperfections. It is difficult to quantify the vertical size exactly (due to the combined effect of the aperture and that of the mirror imperfections), yet it seems to be close to the nominal expected size. The latter can be calculated as

$$d_{x,y}^{\rm nom} = \left[s_{x,y}^2 + s_{x,y}'^2 (L_1 + L_2)^2\right]^{1/2}, \qquad (4)$$

where $s_{x,y}$ is the size of the source and $s'_{x,y}$ is the source divergence (Table 1). Table 4 summarizes the calculation of the nominal beam sizes according to equation (4), along with the observed values estimated using the Gaussian fits.

The size of the focused beam for an ideal focusing lens is $d_y = [(L_2 - L_{\rm M})/(L_1 + L_{\rm M})]\, s_y$, which is approximately 24 µm (FWHM) in the present case. The measured size of the focused beam in Fig. 4(*c*) is 47 µm. An estimate of the increase in the focused beam size due to the mirror's spherical aberrations was performed using an expression by Susini (1995). The estimated increase was found to be ∼5 µm. Therefore, the discrepancy between the measured size and that of the ideal lens is dominated by other imperfections of the mirror such as slope errors and micro-roughness.

The measured horizontal size of the beam without focusing is about 1 mm less than the nominal horizontal size. Note that it remains approximately the same in the two conditions, which suggests that the presence of higher radiation harmonics [Fig. 4(*a*)] and imperfections of the X-ray mirror are not the primary reasons for the observed mismatch. The mismatch can be explained by crystal bending due to imperfect mounting. We performed a ray-tracing simulation to quantify the radius of curvature R, which leads to the observed reduction in the horizontal size. The ray tracing was performed for the slightly asymmetric 111 diamond reflection η = 3.3° in the geometry of the experiment (including the beam-limiting aperture, which is a combination of $A_{\rm V}$ and the lateral size of the crystal).[3] Fig. 5 shows the simulated beam profile of the 111 reflector assuming R = 70 m and a concave shape with respect to the incident beam.

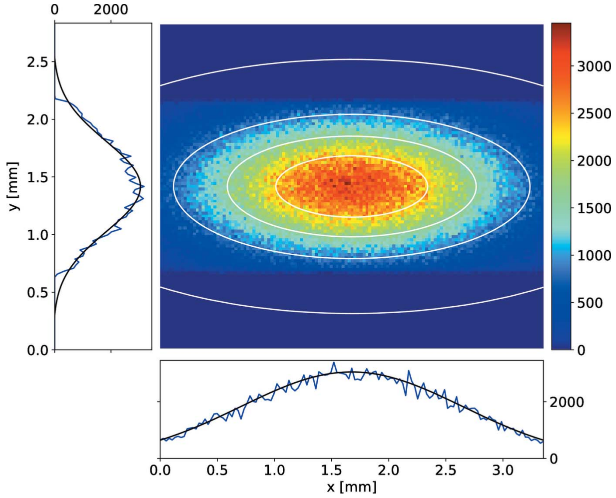

Figure 5
The beam profile on the detector simulated using ray tracing for the 111 reflector with a radius of curvature R = 70 m (concave shape).

The case of the 111 reflector includes known objects and quantities (undulator radiation, a nearly perfect crystal affected by mounting strain, an X-ray mirror and a set of apertures/slits) and where X-ray propagation is well understood using the simple principles of geometric optics and available ray-tracing tools. The estimates and simulations show that the performance characteristics of the 111 reflector are not ideal, but the discrepancies can be explained using realistic imperfections.

---

[3] Note that the limited lateral size of the crystal and the asymmetry of the reflection cannot explain the observed discrepancy.

4.3. CVD diamond Laue reflectors

Scattering from misoriented blocks within an imperfect crystal leads to an increase in the angular divergence, not only in the scattering (horizontal) plane but also in the vertical plane [see *e.g.* Wuttke (2014)]. As a result, the size of the beam profile inevitably increases in both dimensions. At the same time, the integrated reflectivity of the CVD crystal can be greater by an order of magnitude or more (Stoupin *et al.*, 2018). For those experiments which do not require the high energy resolution provided by perfect crystals ($\Delta E/E \simeq 10^{-4}$), an increase in the total available size of the beam can be considered an advantage provided that the flux per unit area (flux density) is not reduced. The resulting enlarged beam can then be limited by an aperture and/or focused on a sample using secondary optics (Stoupin *et al.*, 2019*b*) without a substantial loss in the throughput of the experiment.

The beam profiles of the 220, 131 and 400 CVD diamond Laue reflectors measured in the characterization experiments are shown in Figs. 6(*a*)–6(*c*). These profiles were measured for the beams reflected from the X-ray mirror with the mirror's benders set to minimize the mirror's curvature. Adjusting the positions of the benders in the available motion range in an attempt to focus the beam onto the detector did not yield any appreciable reduction in the beam size. This outcome indicates that the distortion of the radiation wavefront by the CVD diamond reflectors does not permit re-imaging of the radiation source.

The measured profiles are compared with the corresponding beam profiles simulated using ray tracing in perfect crystals in Figs. 6(*d*)–6(*f*). An increase in the characteristic sizes of the beam profiles is observed for the CVD reflectors compared with the profiles of the corresponding perfect-crystal simulations. The sizes of the increased profiles can be reasonably quantified using 2D Gaussian fits, as shown by the side plots in Fig. 6 showing the center slices of the profiles and the corresponding projections of the 2D Gaussian fits. For all profiles in Fig. 6, the corresponding characteristic sizes (FWHM) are summarized in Table 5. The profiles of the 220 and 400 reflectors permit comfortable beamline operations with nearly flat beam profiles slit-limited to 2 × 2 mm.

Table 5
Characteristic dimensions (FWHM) of the beam profiles for the 220, 131 and 400 diamond reflectors: measured using the area detector ($d_x^{\rm e}$, $d_y^{\rm e}$) and simulated using ray tracing for perfect crystals ($d_x^{\rm t}$, $d_y^{\rm t}$).

Reflector	$d_x^{\rm e}$ (mm)	$d_y^{\rm e}$ (mm)	$d_x^{\rm t}$ (mm)	$d_y^{\rm t}$ (mm)
220	4.8	3.1	1.8	0.9
131	3.4	1.2	1.4	0.9
400	4.0	2.4	1.8	0.9

The profile of the 131 reflector [Fig. 6(*b*)] has an obvious tilted appearance. The fits include a rotation angle as a fit parameter. The fitted tilt was approximately 24°. The origin of the rotation of the beam profile appears to be related to the direction of a contour of equal lattice orientation in the corresponding CVD diamond plate, as evident from the results of rocking-curve topography (see supporting information for details). This effect could be useful for tailoring the beam profile to the needs of an experiment at the primary stage of beam monochromatization.

5. Photon flux and energy bandwidth

Table 6 provides a summary of the measured energy bandwidth $\Delta E^{\rm e}$ and the photon flux $F^{\rm e}$ along with the values from

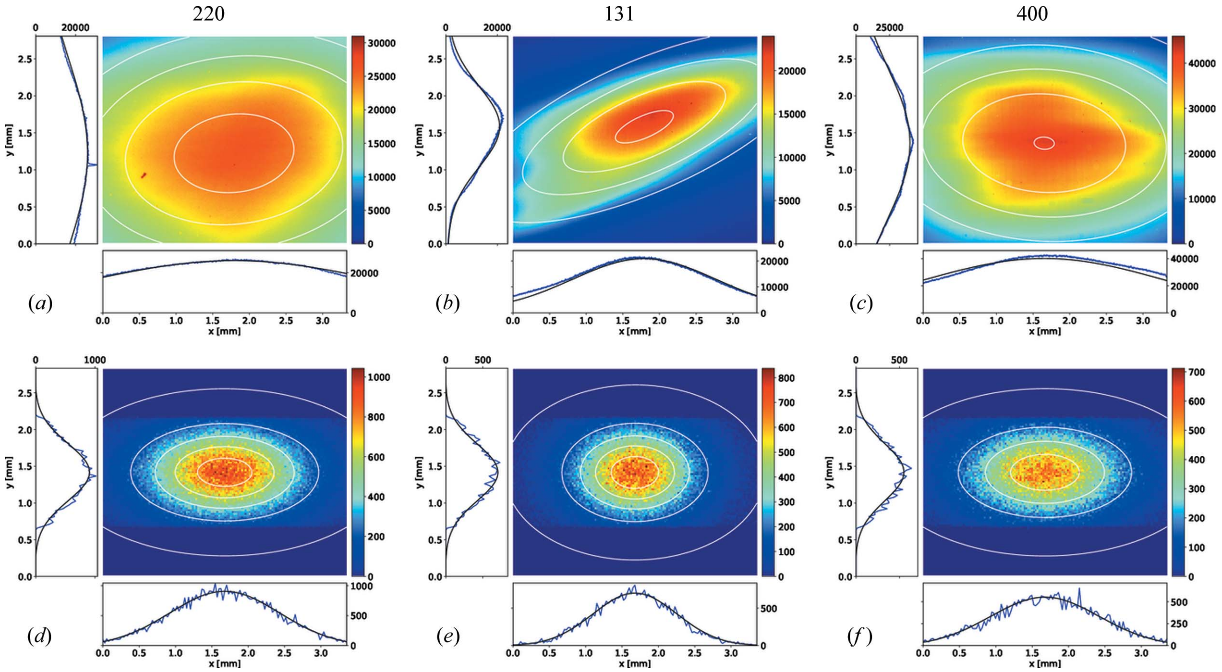

Figure 6
(*a*)–(*c*) Beam profiles of the 220, 131 and 400 CVD diamond Laue reflectors measured using the area detector, and (*d*)–(*f*) beam profiles of the corresponding reflectors simulated using ray tracing for perfect crystals.

Table 6
Summary of 3B beamline characterization parameters (S_0 and S_1 slit gaps set to 2 mm × 2 mm).

K is the undulator parameter, U_n the undulator harmonic, $\Delta E^{\rm t}$ the energy bandwidth (FWHM) from the ray-tracing simulation (perfect-crystal model), $\Delta E^{\rm e}$ the measured energy bandwidth (FWHM), $F^{\rm t}$ the photon flux from the ray-tracing simulation combined with *SPECTRA* calculations, $F^{\rm e}$ the measured photon flux, $G = F^{\rm e}/F^{\rm t} \times A^{\rm t}/A^{\rm e}$ the gain in the photon flux density ($A^{\rm t} = d_x^{\rm t} d_y^{\rm t}$ from Table 5, and $A^{\rm e}$ = 2 × 2 mm). Note that the theoretical (simulated) flux numbers are corrected for the transmission of a high-heat-load limiting filter (0.75 mm of graphite), the transmissivity of a 0.5 mm thick Be window and the reflectivity of the X-ray mirror (~90%).

Reflector	K	U_n	$\Delta E^{\rm t}$ (eV)	$\Delta E^{\rm e}$ (eV)	$F^{\rm t}$ (photons per second)	$F^{\rm e}$ (photons per second)	G
111	2.32	3	2.8	1.4 (0.5)	1.9×10^{12}	1.3×10^{12}	NA
220	2.35	5	4.0	9 (1)	6.9×10^{11}	4.3×10^{12}	2.5
131	2.11	5	5.5	12 (3)	3.5×10^{11}	2.2×10^{12}	2.0
400	2.08	6	6.2	22 (1)	2.2×10^{11}	1.7×10^{12}	3.1

the ray-tracing simulations ($\Delta E^{\rm t}, F^{\rm t}$). It also provides the undulator K parameters and the undulator harmonics U_n chosen to maximize the undulator output at the corresponding operating photon energies of the reflectors. As mentioned above, due to the high quality of the crystal, the 111 reflector case represents an important benchmark in the analysis of the resulting values. From the comparison of the experimental and simulated bandwidths, it appears that the measurement method somewhat underestimates the ray-tracing result of 2.8 eV (derived for a crystal with a radius of curvature R = 70 m). At the same time, the measured photon flux is about 40% less than the simulated value. This mismatch could be related to a number of factors, including non-ideal performance of the undulator and non-ideal alignment of all individual optical components to the common optical axis. Thus, further analysis should take into account possible underestimation of the photon bandwidth and the maximum available photon flux. Nevertheless, the measured value of the photon flux corresponding to the CVD reflectors is greater by a factor of at least 6. A comparative metric that is more relevant for the purpose of performance evaluation is the flux density gain $G = F^{\rm e}/F^{\rm t} \times A^{\rm t}/A^{\rm e}$, where $A^{\rm t} = d_x^{\rm t} d_y^{\rm t}$ (from Table 5) and $A^{\rm e}$ = 2 mm × 2 mm. The flux density gain is reported in the last column of Table 6. The calculation takes into account the characteristic sizes of the simulated beams, which are less than 2 mm × 2 mm (see Table 5).

6. Applications

Recent experiments conducted on the 3B beamline were focused on a direct–ink–write 3D printing process using epoxy-nanoclay fiber-reinforced composites. These studies serve as an example to illustrate the capabilities and range of applicability for the beamline. Among the relevant experiments conducted on the 3B beamline, some were focused on fiber alignment kinetics during 3D printing (Croom *et al.*, 2021), while others were focused on studies of the filler morphology of the printed parts (Trigg *et al.*, 2021).

Fig. 7 (top) shows a schematic of the 3D printing process, involving an ink-extruding nozzle where fiber alignment was investigated using *in situ* X-ray radiography/phase-contrast imaging (PCI), and the printed roadmap where the morphology of the cross section was investigated using small-angle X-ray scattering (SAXS) in raster-scanning mode.

The *in situ* X-ray radiography/PCI was performed using the 15.9 keV X-ray beam of the 220 CVD diamond reflector. Sequences of images were acquired using an ANDOR Neo 5.5 CMOS area detector equipped with an LuAG:Ce scintillator crystal using frame rates up to 25 frames per second. The nominal pixel size of the area detector, taking into account the 5× optical magnification, was 1.3 µm. The velocity field was determined using particle-image velocimetry (PIV), which evaluated the motion of fibers through the nozzle (Willert & Gharib, 1991). Accurate PIV measurement with a spatial resolution of ~100 µm was demonstrated under flow conditions with velocities up to 2.7 mm s^{-1}. Fig. 7(a) shows an example of the calculated velocity field near the tip of the nozzle, superimposed on a selected detector frame (radiograph).

The SAXS mapping of the roadmap's cross section on the microscale was performed using the 9.7 keV X-ray beam of the 111 diamond reflector. A secondary focusing optics (compound refractive lens) was used to create an ~2.5 × 10 µm beam with a photon flux of approximately 10^{10} photons s^{-1}. The SAXS data were collected by a Pilatus

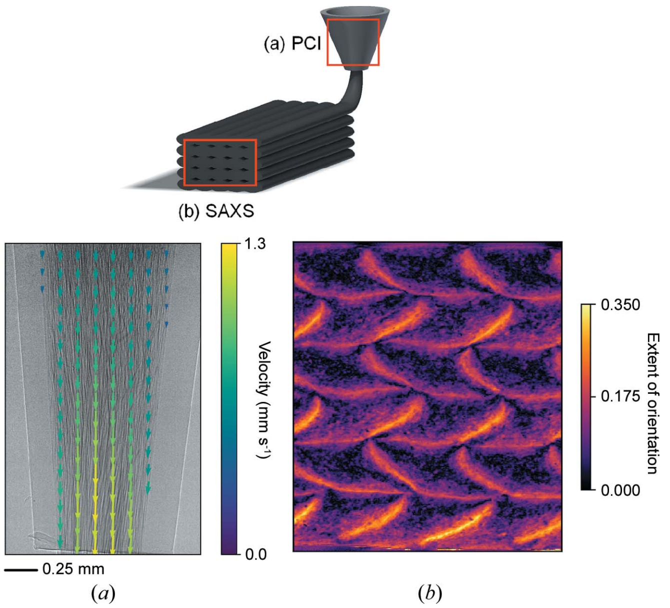

Figure 7
Studies of a direct–ink–write 3D-printing process using epoxy-nanoclay fiber-reinforced composites, which illustrates the beamline capabilities. (Top) A schematic of the process involving an ink-extruding nozzle where fiber alignment kinetics was investigated using *in situ* X-ray radiography/phase-contrast imaging (PCI), and the printed roadmap where the morphology of the cross section was investigated using small-angle X-ray scattering (SAXS). (a) An example of the calculated velocity field near the tip of the nozzle, superimposed on a selected frame (radiograph). (b) A map of the cross section, showing the extent of nanoplatelet orientation extracted from the SAXS dataset.

200K detector using a ‘flyscan’ mode, in which the sample was translated continuously in the vertical direction while the detector was triggered at each 5 µm (0.1 s) interval. Each vertical sweep of the sample was followed by a horizontal sample translation and vertical carriage return. The mapped area was 1.82 mm × 1.55 mm (vertical × horizontal). Each 2D map took approximately 3.5 h to complete. Fig. 7(*b*) shows the image of the cross section where the mapped parameter is the extent of nanoplatelet orientation extracted from the SAXS dataset (Trigg *et al.*, 2021).

These recent experiments were performed while the storage ring was operated at a positron current of 50 mA. Further enhancements to the *in situ* beamline capabilities due to improved image statistics are anticipated upon the planned transition to storage-ring operations at 200 mA.

7. Summary

In summary, we have reported on the design and implementation of beamlines featuring side-bounce (single-reflection) diamond monochromators at the Cornell High Energy Synchrotron Source. Undulator radiation is monochromated using an interchangeable set of diamond crystal plates reflecting radiation in the horizontal (synchrotron) plane, where each crystal plate is set to one of the low-index Bragg reflections 111, 220, 311 or 400. At the nominal Bragg angle of 18° these reflections deliver monochromated X-rays with photon energies of 9.7, 15.9, 18.65 and 22.5 keV, respectively. The 111 reflector is a nearly perfect diamond crystal plate implemented in the Bragg (reflection) geometry, while the remaining reflectors are selected high-dislocation-density single-crystal CVD diamond plates implemented in the Laue (transmission) geometry.

The case of the 111 reflector serves as a benchmark to compare the results of experimental measurements of the reflected beam characteristics (size of the beam profile, photon flux and energy bandwidth) and those of ray-tracing simulations. A reasonable agreement is demonstrated. In the other cases [crystal plates oriented in the Laue (transmission) geometry] it is shown that the use of the pre-selected CVD diamond plates yields a two- to three-fold enhancement in the flux density of the monochromated beam in comparison with the simulated flux density delivered by a perfect crystal. This enhancement is accompanied by an increase in the energy bandwidth, which can be tolerated by a large number of synchrotron experiments (*e.g.* radiography, small- and wide-angle X-ray scattering, or X-ray fluorescence). At the same time, the enlarged sizes of the beam profiles provided by the CVD crystals (resulting from the increased angular divergence upon reflection from an imperfect high-dislocation-density crystal lattice) can be considered an advantage for certain experiments (*e.g.* an enlarged field of view in radiography).

In this work, beamline characterization was performed while the storage ring was operated at a positron current of 50 mA. No indication of a substantial change in the monochromators’ performance was found during more recent tests conducted at 125 mA. A four-fold increase in the reported value of the photon flux is anticipated at the final stage of the storage-ring commissioning where it will be routinely operated at 200 mA. Thus, the photon flux of the monochromated beam could reach values as high as 1×10^{13} photons s^{-1} in certain cases.

During the facility upgrade, two similar beamlines were implemented featuring slightly different monochromator-to-sample distances. At present, one of the implemented beamlines hosts the Functional Materials program, where X-ray scattering and X-ray imaging methods are used to perform materials research (*e.g.* studies of the direct–ink–write 3D-printing process).

Acknowledgements

The authors are grateful to H. Koerner (AFRL) for encouragement, stimulating interest and discussions. We acknowledge the efforts of CHESS staff on the construction of the beamlines. The effort of A. V. Kolyadin (New Diamond Technology) on the manufacturing and timely delivery of the HPHT diamond crystal plates is greatly appreciated. We thank E. Fontes, J. Brock and E. Arenholz for their support and encouragement.

Funding information

This work is based upon research conducted at the Cornell High Energy Synchrotron Source (CHESS) which is supported by the National Science Foundation under award DMR-1332208, and upon research conducted at the Materials Solutions Network at CHESS (MSN-C) which is supported by the Air Force Research Laboratory under award FA8650-19-2-5220. Support for the Cornell Center for Materials Research facility used in this work was provided through NSF Grant DMR-1719875, part of the NSF MRSEC Program. This research used resources of the Advanced Photon Source, a US Department of Energy (DOE) Office of Science User Facility operated for the DOE Office of Science by Argonne National Laboratory under Contract No. DE-AC02-06CH11357. This research was performed while E. B. Trigg and B. P. Croom held an NRC Research Associateship award at the Air Force Research Laboratory.

References

Als-Nielsen, J., Freund, A., Grübel, G., Linderholm, J., Nielsen, M., del Rio, M. & Sellschop, J. (1994). *Nucl. Instrum. Methods Phys. Res. B*, **94**, 306–318.

Batterman, B., Shastri, S. & Richter, D. (2021). *Energy Resolution and Angular Divergence Measurement for Monochromatic Synchrotron Radiation*, https://www.chess.cornell.edu/users/calculators/x-ray-calculations-energy-analyzer.

Bilderback, D. H., Freund, A. K., Knapp, G. S. & Mills, D. M. (2000). *J. Synchrotron Rad.* **7**, 53–60.

Bowen, D. K. & Tanner, B. K. (1998). Editors. *High Resolution X-ray Diffraction and Topography.* London: Taylor and Francis.

Croom, B. P., Abbott, A., Kemp, J. W., Rueschhoff, L., Smieska, L., Woll, A., Stoupin, S. & Koerner, H. (2021). *Additive Manufacturing*, **37**, 101701.

Dippel, A.-C., Liermann, H.-P., Delitz, J. T., Walter, P., Schulte-Schrepping, H., Seeck, O. H. & Franz, H. (2015). *J. Synchrotron Rad.* **22**, 675–687.

Gomez, A., Dina, G. & Kycia, S. (2018). *Rev. Sci. Instrum.* **89**, 063301.

Grübel, G., Abernathy, D., Vignaud, G., Sanchez del Rio, M. & Freund, A. (1996). *Rev. Sci. Instrum.* **67**, 3349.

Hubbell, J. & Seltzer, S. (2004). *NIST Standard Reference Database 126: X-ray Mass Attenuation Coefficients*. https://physics.nist.gov/PhysRefData/XrayMassCoef/tab3.html.

Jiang, Z., Li, X., Strzalka, J., Sprung, M., Sun, T., Sandy, A. R., Narayanan, S., Lee, D. R. & Wang, J. (2012). *J. Synchrotron Rad.* **19**, 627–636.

Juanhuix, J., Gil-Ortiz, F., Cuní, G., Colldelram, C., Nicolás, J., Lidón, J., Boter, E., Ruget, C., Ferrer, S. & Benach, J. (2014). *J. Synchrotron Rad.* **21**, 679–689.

Lennie, A. R., Laundy, D., Roberts, M. A. & Bushnell-Wye, G. (2007). *J. Synchrotron Rad.* **14**, 433–438.

Macrander, A., Erdmann, M., Kujala, N., Stoupin, S., Marathe, S., Shi, X., Wojcik, M., Nocher, D., Conley, R., Sullivan, J., Goetze, K., Maser, J. & Assoufid, L. (2016). *AIP Conf. Proc.* **1741**, 030030.

Revesz, P. (2007). *Ion Chamber Flux Calculator*. https://www.chess.cornell.edu/users/calculators/ion-chamber-flux-calculator.

Sagan, D. (2006). *Nucl. Instrum. Methods Phys. Res. A*, **558**, 356–359.

Sanchez del Rio, M., Grübel, G., Als–Nielsen, J. & Nielsen, M. (1995). *Rev. Sci. Instrum.* **66**, 5148–5152.

Shanks, J., Barley, J., Barrett, S., Billing, M., Codner, G., Li, Y., Liu, X., Lyndaker, A., Rice, D., Rider, N., Rubin, D. L., Temnykh, A. & Wang, S. T. (2019). *Phys. Rev. Phys. ST Accel. Beams*, **22**, 021602.

Stoupin, S., Krawczyk, T., Liu, Z. & Franck, C. (2019*a*). *Crystals*, **9**, 396.

Stoupin, S., Krawczyk, T., Ruff, J. P. C., Finkelstein, K. D., Lee, H. H. & Huang, R. (2019*b*). *AIP Conf. Proc.* **2054**, 060019.

Stoupin, S., Ruff, J. P. C., Krawczyk, T. & Finkelstein, K. D. (2018). *Acta Cryst.* A**74**, 567–577.

Stoupin, S., Shvyd'ko, Yu., Trakhtenberg, E., Liu, Z., Lang, K., Huang, X., Wieczorek, M., Kasman, E., Hammonds, J., Macrander, A. & Assoufid, L. (2016). *AIP Conf. Proc.* **1741**, 050020.

Stoupin, S., Terentyev, S. A., Blank, V. D., Shvyd'ko, Y. V., Goetze, K., Assoufid, L., Polyakov, S. N., Kuznetsov, M. S., Kornilov, N. V., Katsoudas, J., Alonso-Mori, R., Chollet, M., Feng, Y., Glownia, J. M., Lemke, H., Robert, A., Sikorski, M., Song, S. & Zhu, D. (2014). *J. Appl. Cryst.* **47**, 1329–1336.

Susini, J. (1995). *Opt. Eng.* **34**, 361–376.

Tanaka, T. & Kitamura, H. (2001). *J. Synchrotron Rad.* **8**, 1221–1228.

Temnykh, A., Dale, D., Fontes, E., Li, Y., Lyndaker, A., Revesz, P., Rice, D. & Woll, A. (2013). *J. Phys. Conf. Ser.* **425**, 032004.

Temnykh, A., Dale, D., Fontes, E., Lyndaker, A., Li, Y., Ruff, J., Revesz, P. & Woll, A. (2016). *AIP Conf. Proc.* **1741**, 020003.

Trigg, E. B., Hmeidat, N. S., Smieska, L. M., Woll, A. R., Compton, B. G. & Koerner, H. (2021). *Additive Manufacturing*, **37**, 101729.

Willert, C. & Gharib, M. (1991). *Exp. Fluids*, **10**, 181–193.

Wuttke, J. (2014). *Acta Cryst.* A**70**, 429–440.

Zhu, D., Feng, Y., Stoupin, S., Terentyev, S. A., Lemke, H. T., Fritz, D. M., Chollet, M., Glownia, J. M., Alonso-Mori, R., Sikorski, M., Song, S., van Driel, T. B., Williams, G. J., Messerschmidt, M., Boutet, S., Blank, V. D., Shvyd'ko, Yu. V. & Robert, A. (2014). *Rev. Sci. Instrum.* **85**, 063106.